



Deformation mechanisms of additively manufactured Hf₁₀Nb₁₂Ti₄₀V₃₈ refractory high-entropy alloy: Dislocation channels and kink bands

Bing Su ^{a,b}, Yanyan Zhu ^{a,b}, Yansong Zhang ^{a,b}, Zuo Li ^{a,b,*}, Fang Cheng ^{a,b,c}, Shisong Li ^{b,c,d}

^a School of Materials Science and Engineering, Beihang University, Beijing, 100191, China

^b National Engineering Laboratory of Additive Manufacturing for Large Metallic Components, Beijing, 10091, China

^c School of Aeronautics and Astronautics, Tiangong University, Tianjin, 300387, China

^d Research Institute of Aero-Engine, Beihang University, Beijing, 100191, China



ARTICLE INFO

Keywords:

Additive manufacturing
Microstructure
Mechanical properties
Refractory high-entropy alloy

ABSTRACT

To date, the reported refractory high-entropy alloys (RHEAs) with strength and ductility synergy all have up to 1 GPa strain hardening rate (SHR). Keeping the SHR of more than 1 GPa in the RHEAs can postpone the point of plastic instability, thus prolonging the uniform tensile ductility (UTD). In this paper, Hf₁₀Nb₁₂Ti₄₀V₃₈ RHEA with high strength and ductility is successfully manufactured by laser-directed energy deposition (L-DED). The yield strength of the alloy is about 1011 MPa with the tensile ductility of ~12.6 %. Interestingly, the SHR of the alloy is very low, far below 1 GPa. The stress-strain curve of the alloy does not only show no premature dropout, but also exhibits a flat plateau-type curve. For this interesting phenomenon, the deformation mechanisms of Hf₁₀Nb₁₂Ti₄₀V₃₈ alloy are systematically investigated by investigating the deformation microstructures. The results indicate that the dislocation modes are diversifying, but the limited number of tangles generated by the intersection of dislocation channels are the main source of SHR. Various dislocation configurations such as single dislocation channel and cross-slip are stimulated sequentially, and although they have no positive effect on the SHR of the alloy, they allow alloy to accommodate plastic deformation. Combined with the kink bands as a strain softening mechanism, it improves the ductility while decreasing the SHR. Multiple dislocation channels interactions and kink bands are clearly identified as the two deformation mechanisms governing strain hardening and strain softening. The competition between two mechanisms generates the phenomenon mentioned above. This study does not only shed new insights on the unique deformation behavior of Hf₁₀Nb₁₂Ti₄₀V₃₈ RHEA but also complement the current general perception about the relationship between SHR and ductility of RHEAs.

1. Introduction

High-entropy alloys (HEAs), consist of many constituent elements with unrestricted content, can explore better mechanical properties owing to their compositional flexibility than conventional alloys [1–4]. Among the HEAs, body-centered cubic (bcc) refractory high-entropy alloys (RHEAs) exhibit high strength, some even over 1 GPa [5–7]. However, their low-to-no tensile plasticity at ambient temperature hinders the processability and limits the engineering applications [8,9]. To date, researchers have proposed various methods to overcome the strength-ductility trade-off [1,10,11]. On the premise of guaranteeing the strength of RHEAs, the problem of room-temperature plasticity of RHEAs is being gradually solved [12–14]. For instance, the introduction

of heterogeneities into HfNbTiV RHEA alters the dislocation plane slip mode to promote strain hardening and simultaneous enhancement of strength and plasticity [2,10]. Besides, local chemical order (LCO) in Ti-Zr-V-Nb-Al bcc HEA promotes dynamic hardening. Adequate work-hardening rate (WHR) effectively enhances the ductility [11]. In addition, the formation of hierarchical chemical fluctuations (HCFs) in Al₁₀HfNbTiV RHEA gives rise to several unusual strain-hardening rate upturns, achieving a synergistic combination of high strength and large ductility [1].

Above mentioned refractory high-entropy alloys with strength and ductility synergy have one common characteristic: high strain hardening rate. Their strain hardening rates are generally 1 GPa or more [1,10,11]. The strain hardening rate Θ (SHR, $\Theta = d\sigma_t/d\varepsilon_t$) is the slope of the true

* Corresponding author. School of Materials Science and Engineering, Beihang University, Beijing, 100191, China.

E-mail address: lizhuo@buaa.edu.cn (Z. Li).

stress-strain curve [15–18]. It usually determines the ductility of the alloy (especially uniform tensile ductility, UTD) [19–21]. The intersection of SHR and true stress (σ_t) corresponds to the point of plastic instability, after which necking occurs [15,22]. The low SHR leads to an early plastic instability. Once plastic instability such as necking occurs, such severely localized flow can trigger severe damage rather than spreading the strain over the entire sample [23]. And then the alloy tends to generate stress concentrations, UTD degradation and undergo fracture failure [11,24]. Instead, the high SHR can postpone the point of plastic instability, thus prolonging UTD and solving the “strength-ductility trade-off” [1,23,25,26]. So, is there a clear value range to classify low strain-hardening rate and high strain-hardening rate? Most studies have suggested that the high strain-hardening rate should be at least above 1 GPa, and some even above 2 GPa [1,23]. <Nature> has reported that keeping the strain-hardening rate Θ of more than 1 GPa over a wide range in the RHEAs can achieve a good synergy of yield strength and UTD [1]. For example, the strain-hardening rate of Al₁₀HfNbTiV alloy reaches about 1300 MPa in the uniform plastic deformation stage, thus achieving a combination of high yield strength (1390 MPa) and tensile strain to failure (20 %) [1]. However, the SHR of AlHfNbTiTa [1] is below 1000 MPa and it has a low-to-no tensile ductility (~3 %). Likewise, Al₅HfNbTiTa [1] alloy has less than 1000 MPa SHR and tensile strain to failure is even lower than 2.5 %.

Most RHEAs are currently prepared by vacuum arc melting (VAM) [6]. Due to the high melting points of the refractory elements and the huge differences in melting points between the elements, VAM ingots need to be flipped and remelted at least five times to ensure the chemical homogeneity [8,27,28]. It also typically leads to macro-segregation in the RHEAs prepared by VAM. While laser-directed energy deposition

(L-DED) enables rapidly melt high melting point elements by using the high energy density of the laser beam. The ultrafast cooling rates minimized the compositional partitioning [8]. Li et al. [29] compared the NbMoTa alloys manufactured by L-DED and VAM and found that the former has smaller component microscopic segregation. Su et al. [6] demonstrated that the L-DED AlMo_{0.5}NbTa_{0.5}TiZr alloy not only exhibits comparable high-temperature strength to the VAM alloy, but also has higher microhardness while avoiding macro-segregation. In summary, L-DED is a prospective alternative for the rapid and low-cost fabrication of RHEAs.

In this work, Hf₁₀Nb₁₂Ti₄₀V₃₈ RHEA with high tensile strength and ductility was successfully fabricated by L-DED. The Hf₁₀Nb₁₂Ti₄₀V₃₈ alloy has outstanding mechanical properties (tensile yield strength~1011 MPa and ductility~12.6 %) even at a low strain hardening rate (around 500 MPa). It is unique that Hf₁₀Nb₁₂Ti₄₀V₃₈ alloy exhibits low strain hardening rate but high ductility. The phenomenon in our alloy is contradictory to the high strain-hardening rate effect that is currently widespread recognition in RHEAs. Similar phenomena have been observed in other alloys such as beta titanium-based alloys [30]. For this mechanical behavior of β -titanium, researchers have proposed the dislocation-free “giant fault”, stress-induced ω -phase, microbands and other deformation theories. However, the above-mentioned mechanisms are not completely suitable in RHEAs. The underlying mechanism of this interesting plastic deformation in RHEAs is unclear. Hence our work aims to evaluate the tensile properties of this new RHEA and to understand the underlying deformation mechanisms, providing a guiding for subsequent alloy design.

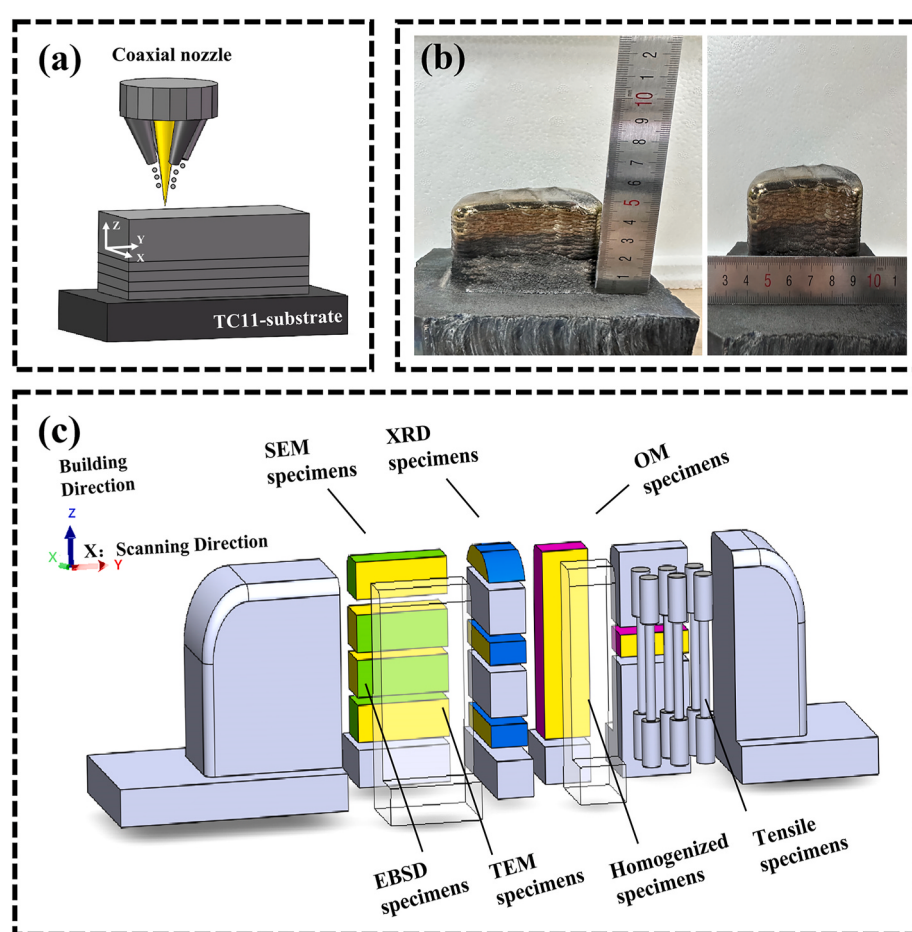


Fig. 1. (a) Schematic illustration of the L-DED process. (b) Macroscopic photos of Hf₁₀Nb₁₂Ti₄₀V₃₈ sample manufactured by L-DED. (c) Schematic illustration of different test specimens.

2. Experimental procedures

2.1. Alloy preparation

The alloys were fabricated from commercially pure (all in 99.9 % wt. %) Hf, Nb, Ti, and V powders by laser-directed energy deposition. These elemental powders were well blended by mechanical mixing. During the forming process, the rolled TC11 was the substrate and $\text{Hf}_{10}\text{Nb}_{12}\text{Ti}_{40}\text{V}_{38}$ was deposited on the top of TC11 as shown in Fig. 1a. The bulk alloy with a 30 mm (SD) \times 50 mm (TD) \times 50 mm (BD) dimension was prepared using a 10 Kw fiber L-DED system in an Ar atmosphere with an O_2 content of less than 50 ppm (Fig. 1b). Due to the presence of a small amount O_2 in the chamber, the alloy shows color variations at different distances from the substrate in the macroscopic photographs as shown in Fig. 1b. The oxidized layers of all samples in the subsequent microstructural and mechanical property evaluations are removed, which has no effect on the validity of the conclusions in the paper. In this paper, X is the laser scanning direction (SD), Z is the laser building direction (BD), and the perpendicular to BD and SD is the transverse direction (TD) Y. The processing parameters were as follows: laser power 4 kW, laser scanning speed 800–1000 mm/min and laser powder feeding rate 18–24 g/min. For simplicity, as-deposited alloy was denoted as Hf10. The elemental composition of the mixed powder and the as-built Hf10 alloy was tested by inductively coupled plasma-atomic emission spectrometry (ICP-AES). The results are listed in Table 1. The difference between the two is insignificant.

2.2. Microstructural characterization

The different specimens were cut from the L-DED block by electrical discharge machining (EDM) as shown in Fig. 1c. Crystallographic constitution was investigated by X-ray diffraction (XRD, D8 DISCOVER). Microstructure and grain orientation were characterized by a scanning electron microscope (SEM, JEOL JSM 7900F). The SEM is equipped with energy dispersive x-ray spectroscopy (EDS) for composition analysis and an electron backscatter diffraction (EBSD) detector. More detailed microstructure at the nano levels was performed by transmission electron microscope (TEM, FEI Tecnai G2 F20).

2.3. Mechanical properties tests

Mechanical properties of the alloy were characterized by quasi-static uniaxial tensile tests at ambient temperature. Tensile specimens were dog-bone shaped as shown in Fig. 1c, with a gauge diameter of 3 mm and a gauge length of 15 mm. The nominal strain rate of $1 \times 10^{-3}/\text{s}$ was used in this study. The samples were tested at least three times to confirm the reproducibility. In addition, interrupted tensile tests at a true strain of $\sim 3.5\%$ and $\sim 8\%$ were performed to investigate the underlying mechanisms during the plastic deformation of Hf10 alloy.

3. Results

3.1. Microstructure and phase constitution

The phase constitution and microstructure of Hf10 RHEA were investigated in detail. Fig. 2a indicates the XRD patterns of Hf10 RHEA. Apart from the primary bcc peaks, Hf10 RHEA exhibits no additional diffraction peaks. Bright-field TEM image and the corresponding selected area electron diffraction of Hf10 RHEA (Fig. 2b) demonstrates

the absence of other crystal phase in the BCC matrix, which is coherent with the XRD patterns. As seen in Fig. 2c, YZ-sectional EBSD inverse pole figure (IPF) map shows the typical L-DED grain morphology. The columnar grains grow along BD, which usually opposes to the maximum heat flowing direction. High cooling rates (10^2 – 10^3 K/s) and the directional heat transfer to the substrate during L-DED result in long and wide columnar grains of Hf10 alloy, which is similar with the grain morphology of most L-DEDded alloy [31]. Through multilayer deposition, the length of columnar grains could be up to several millimeters. EDS analyses are carried out on regions across multiple grain boundaries in the EBSD IPF map, precisely reveal the chemical distribution of Hf10 alloy as shown in Fig. 2c. Obviously, the four principal elements Hf, Nb, Ti, V indicates a spatially uniform distribution at both grain boundaries and grain interiors. The rapid solidification of the alloy during L-DED can effectively reduce the micro-segregation [6], while circulating heat treatment further facilitates their chemical homogenization [32].

As an atomic-scale heterogeneous material, refractory high-entropy alloys possess locally varying compositions and local chemical ordering [5]. It should be noted that the chemical inhomogeneities we discuss here are on the nanoscale rather than on the micrometer or higher scales the commonly discussed, such as segregation in dendritic and inter-dendritic regions [23]. For the possible presence of local chemical fluctuations (LCFs) in Hf10 alloy, deeper insights are revealed by nanoscale characterization. As shown in Fig. 3a, copious LCFs are observed in a single grain of Hf10 alloy. The fine striped wave-structure of these LCFs is roughly 10 nm wide and 40–150 nm long. This modulated structure of Hf10 alloy features high volume fraction and small modulation wavelength. The LCFs structure has a BCC crystal structure like the matrix, and Hf and V are usually enriched in LCFs [10,28,33,34]. The shear strain (ϵ_{yy}) along the [01-1] direction is plotted by the geometric phase analysis (GPA) method and shown in Fig. 3d. LCFs lead to inhomogeneous local strain distribution. The dispersed red regions correspond to the LCFs, which shows a large elastic strain due to the mismatch between the small atomic radius of V and the large atomic radius of Hf. The quantitative curve indicates this elastic strain is larger in the LCFs, ranging from 0.1 % to -0.1% (red dots). The lattice strain is relatively small in the BCC matrix (black dots). The strain in the interface region presents a gradient. The formation of LCFs is driven by enthalpy fluctuations and the enthalpy of Hf10 alloy is -1.1264 kJ/mol [1]. The negative mixing enthalpy of Hf10 alloy generates LCFs, which is consistent with the discussion by ref.6. Fig. 3(e-g) show the distorted fringes of the {101}, {110}, and {01-1} plane along the axis of the $[-111]_{\text{bcc}}$ zone axis. The LCFs has different distortion levels and distortion regions in each plane, as shown in Fig. 3e-g. LCFs could alter the local generalized stacking fault energy, thus affecting the dislocation behavior and mechanical properties [35].

3.2. Mechanical properties

The degradation of the tensile ductility of metallic materials at high flow stresses is a consequence of the increased tendency to unstable flow under uniaxial tension [23]. At present, in RHEAs, SHR above 1 GPa can postpone this flow instability and thus enhance the ductility [1]. On the contrary, SHR below 1 GPa is prone to fracture [1]. As shown in Fig. 4ab, the currently reported RHEAs with low SHR fracture before the strain of 4 %. AlHfNbTiTa and $\text{Al}_5\text{HfNbTiTa}$ are the counterexamples in the pursuit of high SHR in <nature>, that is, they have SHR below 1 GPa and exhibit early fracture [1]. The emergence of Hf10 alloy has shattered this common opinion. Fig. 4ab shows the representative true stress-strain curves and the corresponding work hardening rate-strain curves of $\text{Hf}_{10}\text{Nb}_{12}\text{Ti}_{40}\text{V}_{38}$ and other refractory high-entropy alloys. The stress-strain curve of Hf10 indicates a flow stress peak occurs after the onset of plastic deformation, followed by a relatively flat plastic zone. The yield strength of Hf10 is about 1011 MPa with the failure strain of 12.6 %. However, the work-hardening rate of Hf10 alloy is far less than 1 GPa, with a maximum of only 500 MPa. The

Table 1

Elemental composition of the powder and L-DED Hf10 alloy (at%).

Element	Hf	Nb	Ti	V
Powder	10	12	40	38
As-built	10.06	10.34	42.03	37.56

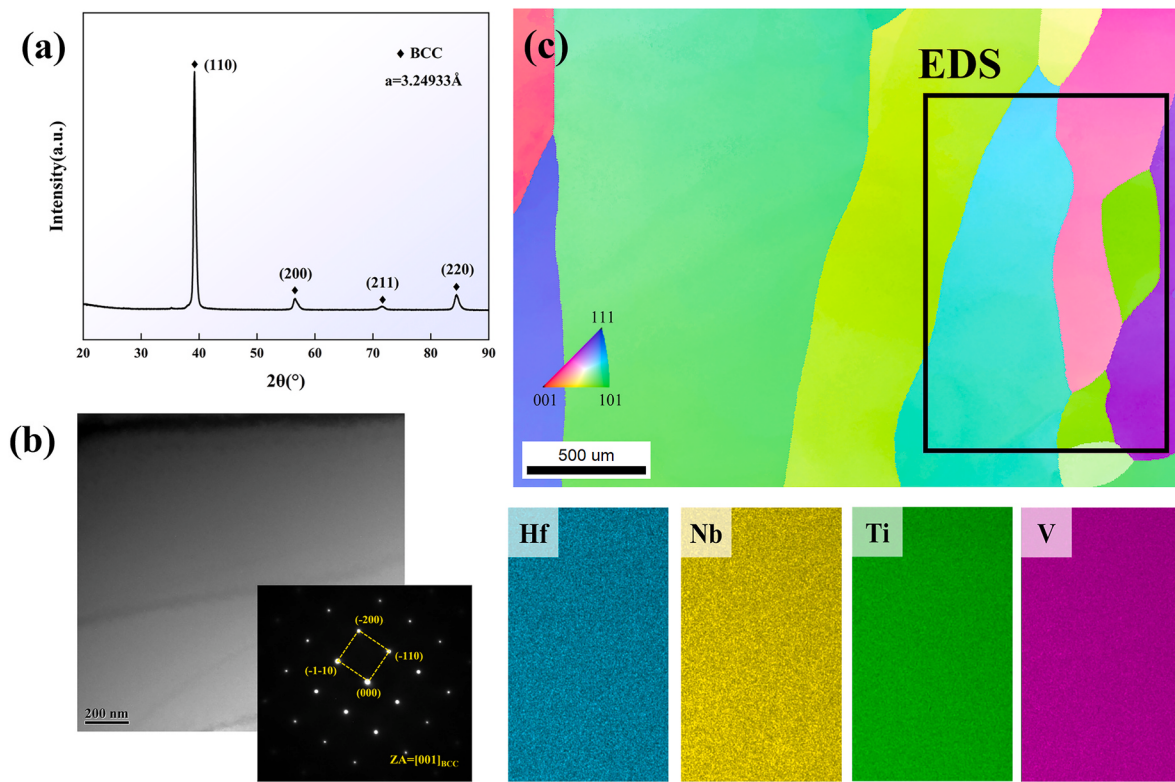


Fig. 2. Complementary meso-scale microstructural characterizations. (a) The XRD patterns of Hf10 RHEA. The lattice constant of the alloy can be calculated to be 3.24933 \AA . (b) Bright-field (BF) TEM image and the corresponding selected area electron diffraction of Hf10 RHEA. (c) YZ-sectional EBSD IPF map and the corresponding element distribution of Hf, Nb, Ti, V with multiple grain boundary regions. IPF map of Hf10 RHEA shows a nearly random texture.

macro-morphology of Hf10 specimens before and after tension also indicates that the strain is uniformly distributed over a large volume of the sample (see Fig. 4c). In summary, the deformation characteristics of Hf10 alloy exhibit excellent ductility but low strain hardening.

We also compare the yield strength and elongation of Hf10 RHEA (marked by red pentagram) with the RHEAs reported in Fig. 4d. Hf10 alloy demonstrates the promising strength-ductility synergy even at a low work-hardening rate, pushing the paradigm for the mechanical properties of L-DDED RHEAs.

3.3. Deformation behavior

The plastic deformation behavior of L-DDED Hf10 alloy could be divided into three stages based on SHR variation (Fig. 4b). In stage I with a true strain of less than 4 %, the strain hardening rate is highest at the beginning of this stage and then decreases rapidly, even below 0 GPa. The decreasing strain hardening rate could be detected in this stage, which may be ascribed to dislocation slip. As the true strain is further increased, for stage II, uniform plastic deformation is observed in the strain range of about 4%–12.1 % and the SHR increases gradually to about 500 MPa on the work hardening rate curve, which is limited but positive. In stage III, when the strain exceeds 12.1 %, the alloy undergoes fracture failure, leading to a decrease in both the stress-strain curve and the work-hardening rate curve. It is well known that the dominant deformation mechanism determines the shape of the strain hardening rate curve. Hence, interrupted tensile tests at $\varepsilon = \sim 3.5\%$ and $\varepsilon = \sim 8\%$ true strains were performed to investigate the primary deformation mechanisms at each stage.

We have performed detailed TEM observations to investigate the dislocation behavior at different stages (Stage I, II, III in Fig. 4b) of plastic deformation. At a strain of 3.5 % (within Stage I), uniformly distributed dislocation dipoles are observed in Hf10 alloy. These dislocation patterns are analogous to the single crystal single-glide. At stage

II, the initial deformation is dominated by planar slip, which tends to form dislocation channels, as shown in Fig. 5b. During further deformation, multiple dislocation channels generate and become entangled. To verify whether there are any other deformation modes (such as phase transformation or twinning) present during the deformation, microstructure of the necking regions in a fractured Hf10 alloy are observed. The SAED pattern (Fig. 5f) indicates there is no martensitic transformation or twinning occurring in the deformation. This suggests that dislocation slip dominates the severe deformation process [13,36]. We observe the heterogeneous deformed microstructure near the tensile fracture by TEM. As shown in Fig. 6a, there are localized bands of high-density dislocations [37]. The dislocations are tangled within the high-density dislocation areas, which can be seen in the magnified TEM image (Fig. 6bc).

We further observe the microstructure at each stage by EBSD to investigate the deformation behaviors. Fig. 7 shows the IPF and the kernel average misorientation (KAM) maps of Hf10 alloy with various strain. Under a 3.5 % strain (Stage I), there are color gradients in the IPF image, which is the result of dislocation slip, illustrated in Fig. 7a₁. At stage II with a strain of 8 %, Hf10 alloy sprout a limited number of lamellas apart from the obvious slip traces, as shown in Fig. 7b₁. As the strain increases, these lamellas extend gradually. Lamellas are distributed inside single grains eventually and they don't penetrate multiple grains (Fig. 7c₁). For further studying these lamellas, we analyzed the misorientation variations along the marked lines in Fig. 8a. The maximum misorientation angle among the strip-matrix interfaces is below 25° (shown in Fig. 8c), which is different from the characteristic misorientation angle 50.5° and 60° for $\{332\} <113>$ twinning and $\{112\} <111>$ twinning in BCC alloy respectively. The formation of smaller misorientations attribute to the presence of kink bands, a common occurrence in titanium and RHEAs [28,38]. The pole figure (PF) maps in Fig. 8d confirms a focused pole in $\{011\}$ PF, with the rest of $\{011\}$ poles, all $\{112\}$ and $\{541\}$ poles rotating around it. This is a

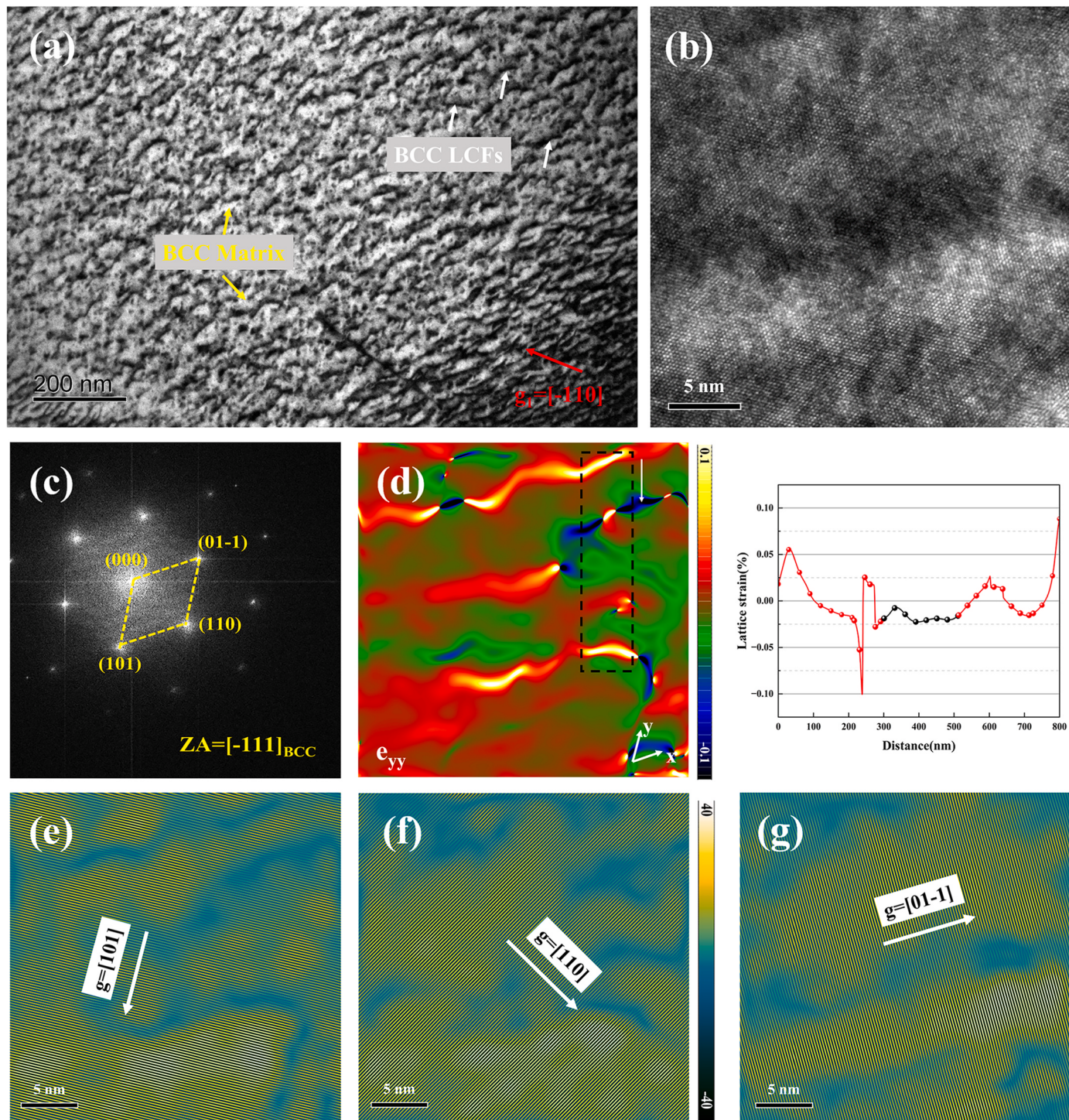


Fig. 3. TEM analysis of the microstructure of Hf10 alloy: (a) BF TEM image. (b) The high-resolution TEM (HRTEM) image from $Z = [-111]$ axis. (c) The SAED patterns through Fast Fourier Transformation (FFT). (d) The corresponding atomic strain map of (b). The curve on the right is the atomic strain distribution in the black rectangular box. For vertical strain (ϵ_{yy}) scales, see the colored bars. (e–g) fringes corresponding to $\{101\}$, $\{110\}$, and $\{01-1\}$, respectively.

typical feature of the PF for the kink band. According to the intra-granular misorientation axis (IGMA) analysis method [37,39], this crystallographic characteristic indicates the existence of kinking surrounding the $<011>$ lattice rotation axis contributed by $<111>\{112\}$ dislocation slip mode.

The kink bands (KBs) formation for Hf10 alloy during tensile is illustrated in Fig. 7d. As the strain increases, dislocations accumulate at grain boundaries where slip and twinning are partially blocked. Inhomogeneous stress between adjacent grains causes grains to rotate to

different directions. Due to differences in the original orientations, the degree of rotation varies among individual grains. Some grains exhibit significant differences in orientation before and after rotation, and kinking is prone to occur in such cases to assist the alloy in adapting to the rotation. Kinking refers to the lattice rotation caused by the slip of dislocations [37]. Areas in one grain drive different slip systems, with different regions rotating to their individual stabilizing stress orientations. This process is achieved by KBs. The KBs rotate at a certain angle around the $<011>$ lattice rotation axis. The misorientation between the

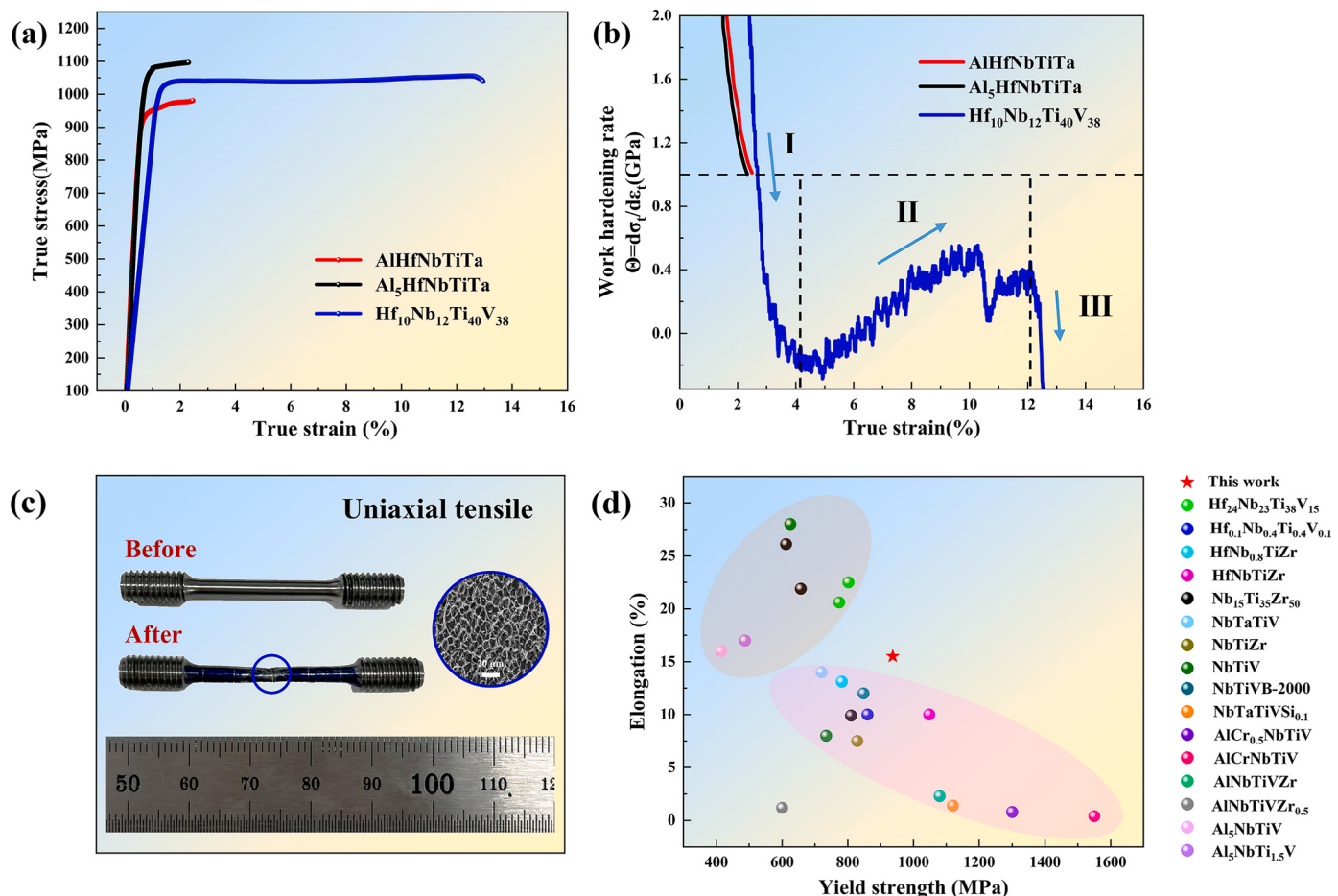


Fig. 4. Mechanical properties of Hf10 RHEA. (a) True stress-strain curves of Hf₁₀Nb₁₂Ti₄₀V₃₈, AlHfNbTiTa [1] and Al₅HfNbTiTa [1] alloys. (b) Corresponding work hardening rate-true strain curves of Hf₁₀Nb₁₂Ti₄₀V₃₈, AlHfNbTiTa [1] and Al₅HfNbTiTa [1] alloys. (c) Macrostructure and fracture morphology of Hf10 specimens before and after uniaxial tension at ambient temperature. (d) Ashby map showing the elongation versus yield strength of refractory high-entropy alloys with various chemical compositions.

matrix and KBs is accommodated in a thin layer (transition bands, TBs). TBs accumulate the higher geometrically necessary dislocation (GNDs). The KAM images (Fig. 7a₁-c₁) show the density of GNDs, indicating the accumulation of dislocations at the spacing of grain boundaries and kink bands. GNDs distribute around kink bands and grain boundaries. This corresponds to our above analysis. The elastic stress fields caused by GNDs superimpose on each other to produce long-range stress. To eliminate the long-range stress, dislocations partially or completely offset the original stress state by moving and rearranging. When they approach each other, dislocations with same signs may generate higher local stress while dislocations with opposite signs help reduce the stress level. Dislocation pairs with opposite sign are distributed symmetrically in TBs to maintain their stability within the crystal, as illustrated in Fig. 7d. This is consistent with other studies [37,40–42]. With further deformation, the existing KBs extend from the concentration of stress to the entire grain or initiate new KBs. Continuous nucleation and propagation of KBs in Hf10 alloy effectively increase the deformability of materials by stress relaxation [37].

4. Discussion

4.1. The origin of low strain hardening

The sources of work-hardening rate for Hf10 alloy are analyzed in detail. Prior to the initiation of plastic deformation, the lattice distortions caused by LCFs can pin dislocations, thus the mobile dislocation

density (ρ_m) of Hf10 alloy is quite low. After the onset of plastic deformation, dislocations multiply rapidly, resulting in a significant increase in ρ_m . A qualitative explanation of the dislocation motion of Hf10 alloy can be provided through the theory of dislocation multiplication [4,43]. The theory can be expressed in a simple formula:

$$\dot{\varepsilon}_p \propto \rho_m \bullet v \bullet b \quad (1)$$

where $\dot{\varepsilon}_p$, ρ_m , v and b refer to the strain rate of plastic deformation, mobile dislocation density, average velocity of dislocation motion and burgers vector, respectively. $\dot{\varepsilon}_p$ can be considered as a constant value in the uniaxial tensile test at ambient temperature. The Burgers vector in BCC crystals is typically $a/2<111>$. V can be calculated using the following equation:

$$v = \left(\frac{\tau}{\tau_0} \right)^{m'} \quad (2)$$

where τ_0 is the required stress for the dislocation to move with unit velocity, τ is the effective shear stress of dislocations, and m' is a stress sensitivity index related to the material. ρ_m increases rapidly, which inevitably leads to v decreasing abruptly. The velocity of dislocation encounter decreases, and SHR does not increase significantly in a short period of time. Meanwhile, the stress τ that the alloy needs to deform drops suddenly, generating the stress landfall. The phenomenon is shown in [Supplementary Fig. 1](#).

In the initial stage of plastic deformation, the elastic interaction

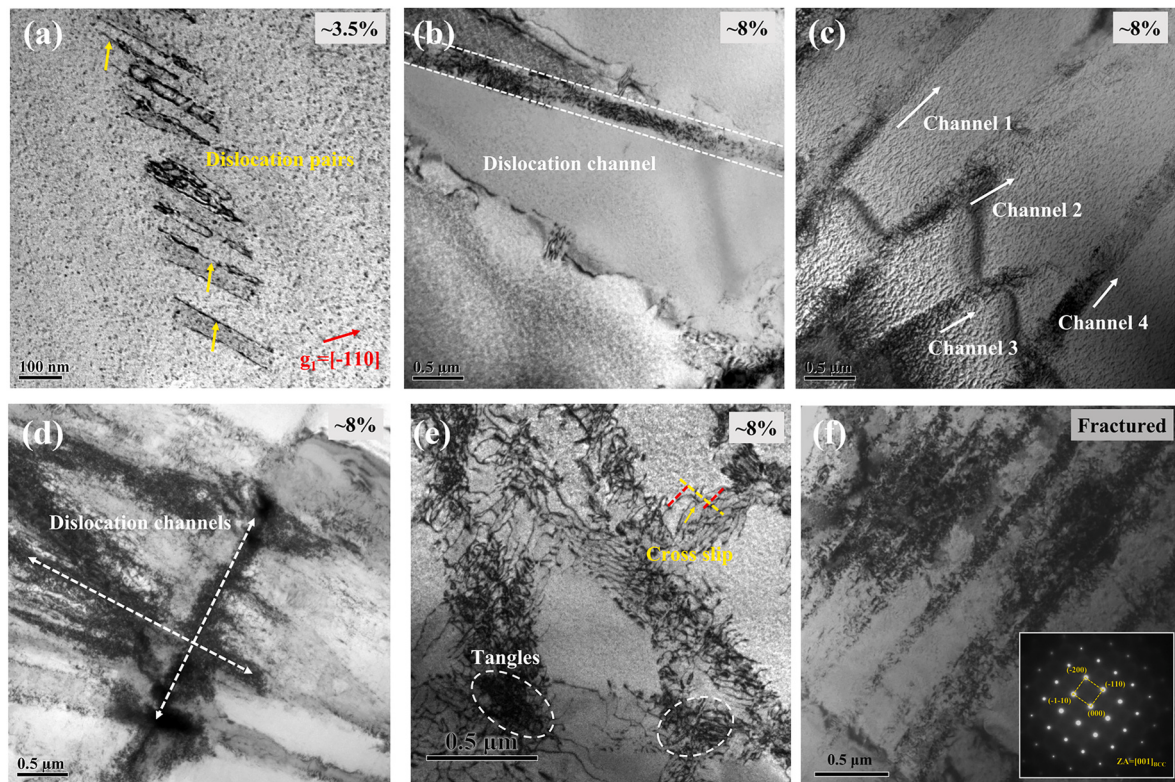


Fig. 5. Evolution of dislocation substructures of Hf10 alloy upon tensile deformation: (a): at a strain of $\sim 3.5\%$. (b)–(e): at a strain of $\sim 8\%$. (f): after tensile fracture.

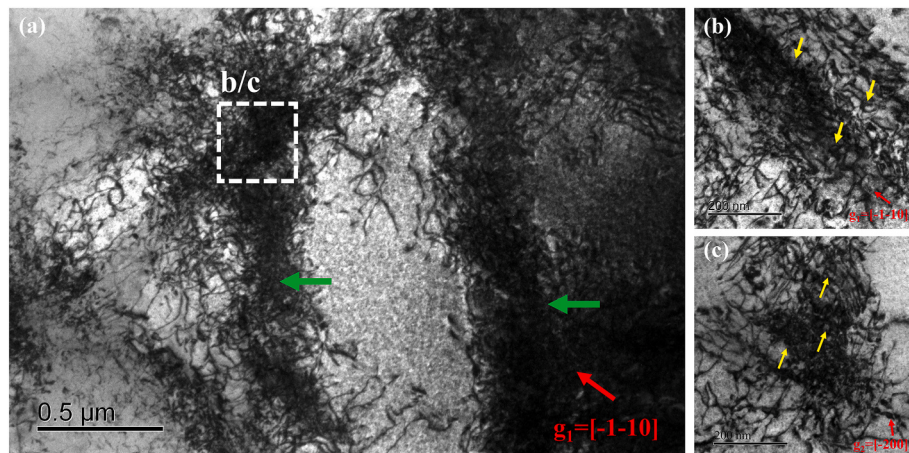


Fig. 6. (a) TEM BF image of Hf10 alloy after tensile fracture, showing high-density dislocation areas, as indicated by green arrows. (b) The magnified image of different regions in the image (a), showing the dislocations are tangled within the high-density dislocation areas, as indicated by the yellow arrows. (For interpretation of the references to color in this figure legend, the reader is referred to the Web version of this article.)

between dislocation dipoles is quite weak and thus the work-hardening rate is low. With increasing strain, the presence of LCFs leads to dislocation channels. The origin of dislocation channels in other BCC RHEAs is slightly different. For example, the dislocation channels in $\text{Al}_{0.3}\text{Nb-Ti}_3\text{VZr}_{1.5}$ alloy are attributed to the ω -phase [8]. The widely distributed LCFs contribute to the critical stress barrier for plasticity initialization [34]. The critical interaction between the first dislocation and the L-CFs result in the redistribution of atoms at the L-CFs. Thus, the lattice distortion is diminished, and the subsequent dislocation motion resistance and energy are simultaneously reduced. The leading dislocations diminish the barrier for continuous dislocation sliding on the same plane, leading to continuous coplanar sliding of the dislocations. Dislocation channels begin to appear, which suggests the “glide plane

softening” during deformation, although there are still many dislocations in the channel [11,34]. Dislocations within one channel tend to drive the same slip system, and this deformation localization feature decreases the frequency of dislocations encountering. The early dislocation channels have no significant positive effect on the strain-hardening rate of Hf10 alloy.

The BCC lattice is not a close-packed structure and lacks a prominent plane with the highest packing density [35]. Its plastic deformation can take place through dislocation slipping on various planes in the $\langle 111 \rangle$ direction, including $\{110\}$, $\{112\}$ and $\{123\}$ planes [35,44,45]. Whereas the widely distributed LCFs cause the change of local energy barrier for dislocation slipping, the preferential slip planes also change, which promotes frequent local cross-slip in Hf10 alloy [35]. Cross-slip

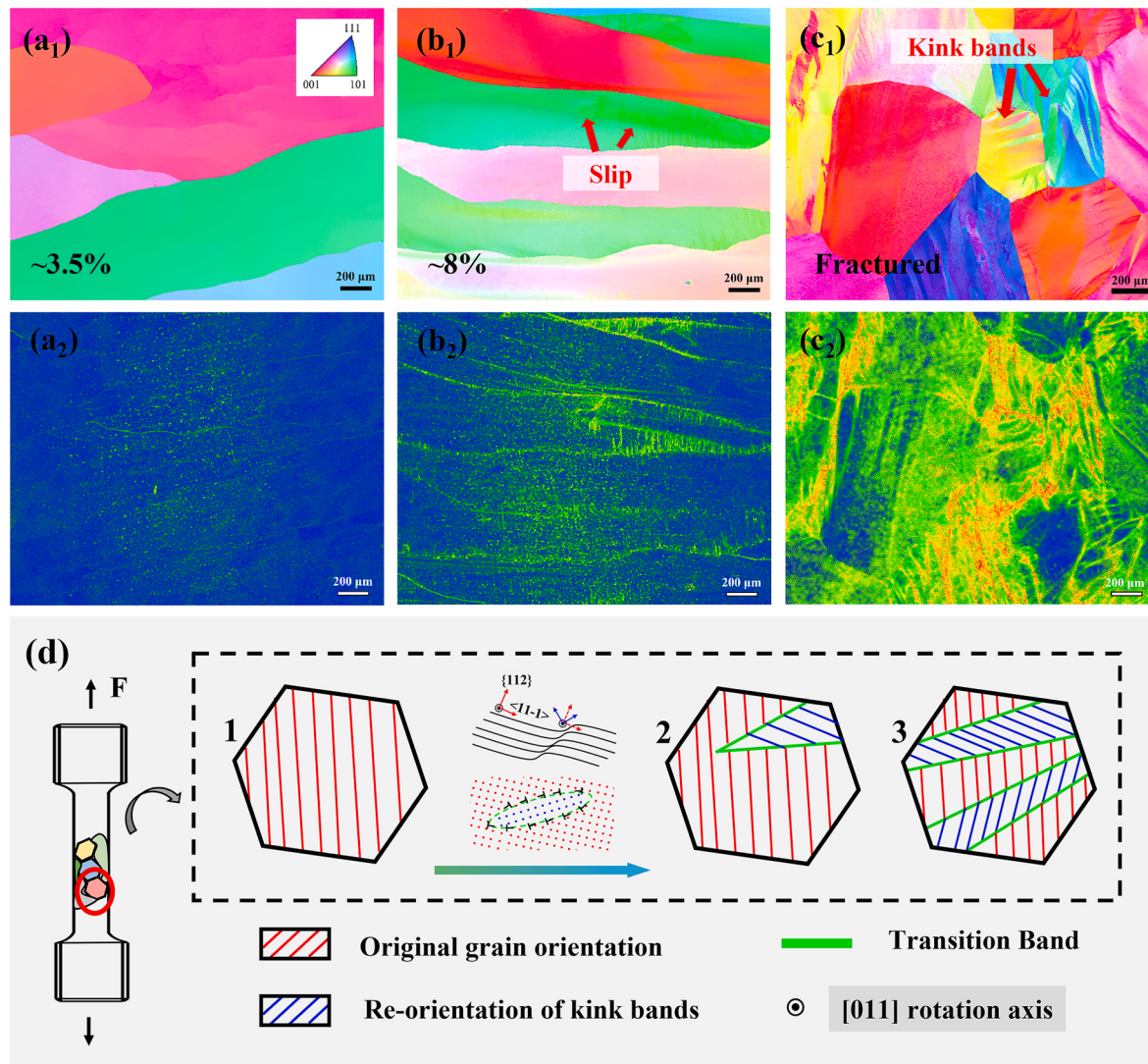


Fig. 7. EBSD IPF and KAM maps of Hf10 alloy at different tensile stages: IPF maps of (a₁) 3.5%-strained specimen, (b₁) 8%-strained specimen and (c₁) the fractured specimen; (a₂), (b₂) and (c₂) are there corresponding KAM maps. (d) Schematic illustration of the kink band deformation in Hf10 alloy.

and double cross-slip are achieved through the blocked screw dislocations motion in Hf10 alloy. High cross-slip frequency promotes dislocation recombination and reduces the rate of dislocation storage [25]. That is, this dynamic recovery contributes to plastic deformation, but is not beneficial to obtain effective work hardening [46]. This is another reason for the low SHR during plastic deformation of Hf10 alloy.

Cross-slip activates multiple dislocation channels. With the ongoing deformation, multiple dislocation channels intersect to form a dislocation network. The network structure of intersecting channels can effectively reduce the mean free range of the mobile dislocations. Meanwhile interactions among the channels inevitably cause dislocations are tangled. Due to the presence of large grains and the absence of second-phase particles, the interfacial strengthening effect is extremely weak. Tangles are the major source of work-hardening rate, although in a low amount.

In summary, there are three reasons for the low work hardening rate of Hf10 alloy. First, the pinning effect of LCFs on dislocations contributes to the low mobile dislocation density. After onset of plastic deformation, average velocity of dislocation motion decreases and the SHR fails to increase in a short time. Second, the dislocation channel reduces the probability of dislocation intersection, which is essentially a softening. Third, despite the emergence of a dislocation network during the later stages of deformation, the quantity of tangles, serving as the main

contributor to SHR, remains restricted. Observing the dislocation behavior in Hf10 alloy (Fig. 5), we find that although the dislocation modes are diversifying, the actual effective hardening is low and late. It can't compensate for the decrease of load-carrying capacity caused by softening, and the tensile strength is still lower than the yield strength. Meanwhile, through comparison with other RHEAs, we think that the fundamental reason of SHR is the interaction between microstructure and dislocations. The quantitative analysis about the magnitude of interaction will be the future research direction.

4.2. The origin of excellent ductility

Despite the SHR of Hf10 alloy is only 500 MPa, the ductility is excellent. Abundant dislocation channels disperse the plastic strains in the narrow deformation bands induced by planar-slip and relieve the stress concentration [11]. Moreover, although the frequent cross-slip is ineffective strain hardening, it facilitates dislocation motion and hence benefits plastic deformation. In addition, kinking that mentioned in section 3.3 is another deformation mode that can coordinate the deformation and produce reorientation. It can effectively accommodate dislocation slip and improve ductility against stress concentration. The above three are all reasons for the reasonable ductility of Hf10 alloy.

It is noteworthy that as a localized inhomogeneous deformation

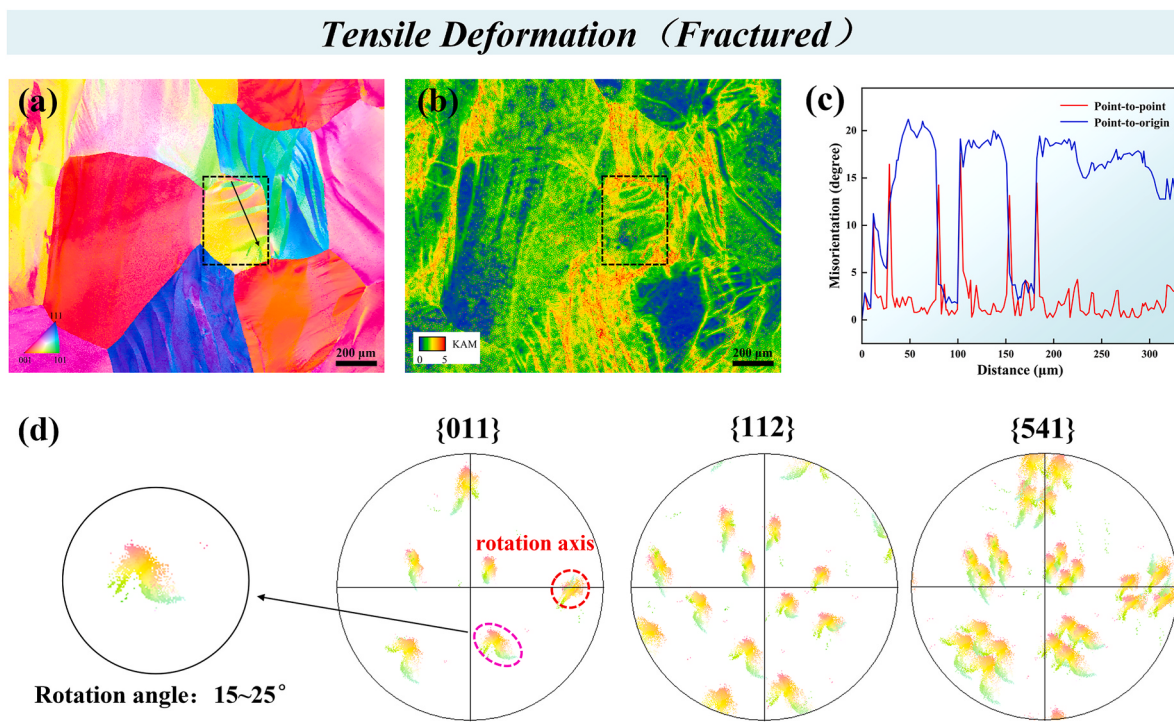


Fig. 8. Fractured Hf10 alloy: (a) inverse pole figure (IPF) of kink bands; (b) KAM map of (a); (c) Misorientation along the line shown in (a); (d) {001}, {112} and {541} pole figures corresponding to the rectangle dotted area in (a).

mode, KBs will lead to strain softening. To some extent, KBs decrease the inherently insignificant work-hardening rate of the Hf10 alloy. Every phenomenon possesses dual nature. Although the absence of a positive impact on SHR, cross-slip and kink bands manifest a remarkable effect on ductility, providing a novel perspective to our understanding of this interesting plastic deformation that is low SHR but large ductility in Hf10 RHEA. A schematic diagram of the dominant deformation mechanism during deformation is shown in Fig. 9. Therefore, it can be suggested that the formation of KBs with a strain softening mechanism occurs simultaneously with the interaction of multi dislocation channels with a strain hardening mechanism [47]. Dislocation channels and kink

bands are common in other BCC RHEAs [8,13,40,42,48]. They conduct an analysis based on the effect of the two mechanisms on the ductility of alloys. The distinction of our work lies in its emphasis on analyzing their impact on the strain hardening rate, offering unique insights to help peers comprehensively understand the two deformation mechanisms. In addition, there are many deformation patterns in Hf10 alloy that have no contribution to the work-hardening rate but are beneficial to ductility, e.g., cross-slip. Altogether, these result in low strain hardening but excellent ductility.

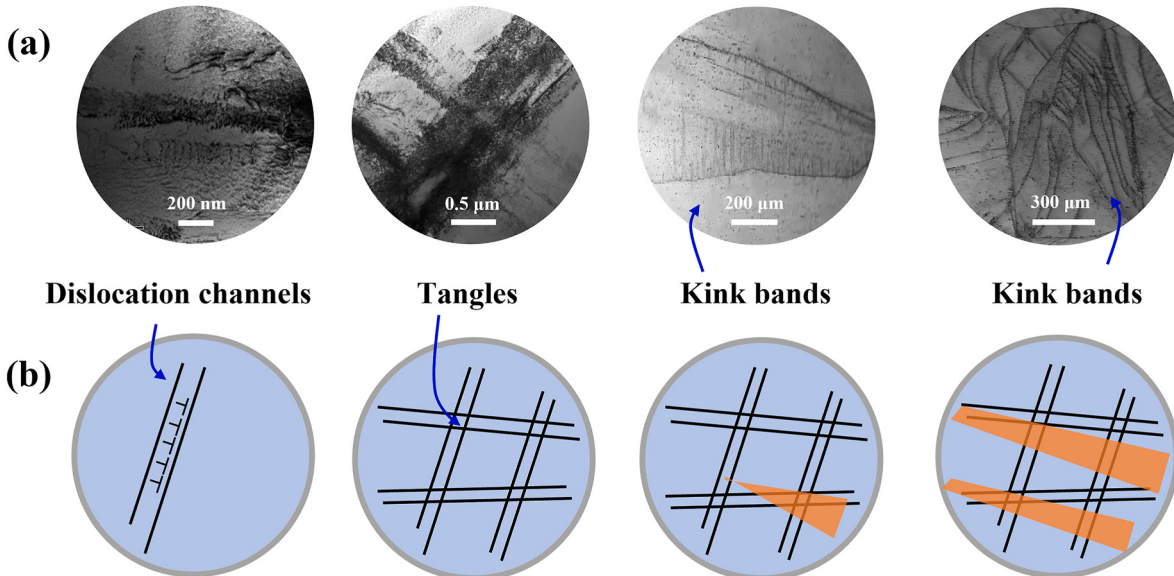


Fig. 9. Schematic illustration of deformation mechanism of Hf10 alloy during tensile at ambient temperature. (a) TEM and Image Quality (IQ) maps during plastic deformation of Hf10 alloy.

5. Conclusions

In summary, Hf₁₀Nb₁₂Ti₄₀V₃₈ (Hf10) refractory high-entropy alloy (RHEA) with high tensile strength and ductility was successfully manufactured by laser-directed energy deposition (L-DED). Hf10 alloy exhibits excellent ductility at a low strain hardening rate (SHR), which is different from the usual RHEAs that fracture at a low SHR. On the basis of this phenomenon, the microstructure of Hf10 alloy and its deformation characteristics during uniaxial tensile strain at ambient temperature are investigated. The main conclusions are as follows.

1. As a single BCC solid solution, the microstructure of L-DEDed Hf10 alloy consists of long and wide columnar grains, which is mainly due to the high cooling rate (10^2 – 10^3 K/s) and the directional heat transfer to the substrate during L-DED process. The rapid solidification and circulating heat treatment during L-DED of Hf10 RHEA facilitate their chemical homogenization and no macro-segregation is found in the Hf10 alloy.
2. The yield strength of Hf10 alloy is about 1011 MPa with the failure strain of 12.6 %. The SHR of Hf10 alloy is only 500 MPa, but the stress-strain curve exhibits a flat plateau-type curve. Hf10 alloy demonstrates a distinctive behavior characterized by superior ductility and a low SHR.
3. Single dislocation channel reduces the probability of dislocation intersection, which is essentially a softening. The tangles, purportedly the main source of work hardening rate, emerges later in the deformation process and occur in relatively low quantities. Collectively, these factors contribute to the low strain hardening rate of Hf10 alloy.
4. The excellent ductility of Hf10 alloy derives from the cross-slip and kink bands. High cross-slip frequency promotes dislocation recombination, which facilitates plastic deformation. And kink bands can effectively accommodate dislocation slip and improve ductility against stress concentration.

The current results not only provide new insights into the unique strength and ductility synergy of RHEAs by L-DED, but also offer innovative solutions with improving of the alloy work-hardening rate. In addition, this paper further complements the current widespread perception of the relationship between SHR and ductility of RHEAs. The three aspects of alloy design, process parameter and subsequent heat treatments to achieve this unique combination of strength and ductility will become a core topic of RHEAs in the future. We expect that the research outcome has significant implications in developing more promising ultra-strong and ductile BCC refractory high-entropy alloys.

CRediT authorship contribution statement

Bing Su: Writing – review & editing, Writing – original draft, Investigation, Funding acquisition, Formal analysis, Data curation, Conceptualization. **Yanyan Zhu:** Writing – review & editing, Validation. **Yansong Zhang:** Writing – review & editing, Supervision, Formal analysis. **Zhuo Li:** Writing – review & editing, Resources, Project administration, Funding acquisition, Data curation. **Fang Cheng:** Writing – review & editing, Data curation. **Shisong Li:** Writing – review & editing, Data curation.

Declaration of competing interest

The author declare no potential conflicts of interest with respect to the research, author-ship, and/or publication of this article.

Data availability

Data will be made available on request.

Acknowledgements

This work was supported by National Key Research and Development Program of China (Grant No.2023YFB4603304).

Appendix A. Supplementary data

Supplementary data to this article can be found online at <https://doi.org/10.1016/j.msea.2024.147247>.

References

- [1] Z. An, A. Li, S. Mao, T. Yang, L. Zhu, R. Wang, Z. Wu, B. Zhang, R. Shao, C. Jiang, B. Cao, C. Shi, Y. Ren, C. Liu, H. Long, J. Zhang, W. Li, F. He, L. Sun, J. Zhao, L. Yang, X. Zhou, X. Wei, Y. Chen, Z. Lu, F. Ren, C.-T. Liu, Z. Zhang, X. Han, Negative mixing enthalpy solid solutions deliver high strength and ductility, *Nature* 625 (2024).
- [2] C. Liu, Y. Wang, Y. Zhang, L.-C. Zhang, L. Wang, Deformation mechanisms of additively manufactured TiNbTaZrMo refractory high-entropy alloy: the role of cellular structure, *Int. J. Plast.* 173 (2024) 103884.
- [3] Y.L. Wang, K.C. Chan, A super strong high entropy alloy with discontinuous precipitation and fine grains by additive manufacturing and thermomechanical treatment, *Mater. Sci. Eng., A* 876 (2023).
- [4] H. Li, S. Gao, Y. Tomota, S. Ii, N. Tsuji, T. Ohmura, Mechanical response of dislocation interaction with grain boundary in ultrafine-grained interstitial-free steel, *Acta Mater.* 206 (2021).
- [5] R. Wang, Y. Tang, Y. Ai, S. Li, L.a. Zhu, S. Bai, Strengthening and ductilization of a refractory high-entropy alloy over a wide strain rate range by multiple heterostructures, *Int. J. Plast.* 173 (2024).
- [6] B. Su, J. Li, C. Yang, Y. Zhang, Z. Li, Y. Zhang, Microstructure and mechanical properties of a refractory AlMo0.5NbTa0.5TiZr high-entropy alloy manufactured by laser-directed energy deposition, *Mater. Lett.* 335 (2023) 133748.
- [7] O.N. Senkov, G.B. Wilks, J.M. Scott, D.B. Miracle, Mechanical properties of Nb₂₅Mo₂₅Ta₂₅W₂₅ and V₂₀Nb₂₀Mo₂₀Ta₂₀W₂₀ refractory high entropy alloys, *Intermetallics* 19 (5) (2011) 698–706.
- [8] Y. Zhang, H. Wang, Y. Zhu, S. Zhang, F. Cheng, J. Yang, B. Su, C. Yang, High specific yield strength and superior ductility of a lightweight refractory high-entropy alloy prepared by laser additive manufacturing, *Addit. Manuf.* 77 (2023).
- [9] C. Tian, D. Ouyang, P. Wang, L. Zhang, C. Cai, K. Zhou, Y. Shi, Strength-ductility synergy of an additively manufactured metastable high-entropy alloy achieved by transformation-induced plasticity strengthening, *Int. J. Plast.* 172 (2024).
- [10] Z. An, S. Mao, T. Yang, C.T. Liu, B. Zhang, E. Ma, H. Zhou, Z. Zhang, L. Wang, X. Han, Spinodal-modulated solid solution delivers a strong and ductile refractory high-entropy alloy, *Mater. Horiz.* 8 (3) (2021) 948–955.
- [11] L. Wang, J. Ding, S. Chen, K. Jin, Q. Zhang, J. Cui, B. Wang, B. Chen, T. Li, Y. Ren, S. Zheng, K. Ming, W. Lu, J. Hou, G. Sha, J. Liang, L. Wang, Y. Xue, E. Ma, Tailoring planar slip to achieve pure metal-like ductility in body-centred-cubic multi-principal element alloys, *Nat. Mater.* 8 (2023).
- [12] J. Zou, X. Fu, Y. Song, T. Li, Y. Lu, Z. Zhang, Q. Yu, High strength and deformation stability achieved in CrCoNi alloy containing deformable oxides, *J. Mater. Sci. Technol.* 134 (2023) 89–94.
- [13] Y. Zhang, Z. Bu, T. Yao, L. Yang, W. Li, J. Li, Novel BCC Ti-Al-Nb-Zr medium-entropy alloys with ultrahigh specific strength and ductility, *J. Alloys Compd.* 936 (2023).
- [14] C. Duan, A. Kostka, X. Li, Z. Peng, P. Kutlesa, R. Pippan, E. Werner, Deformation-induced homogenization of the multi-phase senary high-entropy alloy MoNbTaTiVZr processed by high-pressure torsion, *Mater. Sci. Eng., A* 871 (2023).
- [15] G. Li, M. Liu, S. Lyu, M. Nakatani, R. Zheng, C. Ma, Q. Li, K. Ameyama, Simultaneously enhanced strength and strain hardening capacity in FeMnCoCr high-entropy alloy via harmonic structure design, *Scripta Mater.* 191 (2021) 196–201.
- [16] F. Cheng, H. Wang, Z. Li, X. Cheng, D. Zheng, S. Zhang, X. Hu, H. Zhang, M. Liu, Dynamic compression deformation behavior of laser directed energy deposited $\alpha + \beta$ duplex titanium alloy with basket-weave morphology, *Addit. Manuf.* 61 (2023).
- [17] W. Fu, Y. Sun, G. Fan, Y. Huang, Z. Ning, X. Li, K. Wang, J. Sun, S. Jiang, Strain delocalization in a gradient-structured high entropy alloy under uniaxial tensile loading, *Int. J. Plast.* 171 (2023).
- [18] X.R. Guan, Q. Chen, S.J. Qu, G.J. Cao, H. Wang, X.D. Ran, A.H. Feng, D.L. Chen, High-strain-rate deformation: stress-induced phase transformation and nanostructures in a titanium alloy, *Int. J. Plast.* 169 (2023).
- [19] J. Cui, M. Yang, G. Liu, L. Wang, S. Sun, B. Wang, H. Cai, Y. Xue, Work-hardening ability enhancement of lightweight high entropy alloys via adding yttrium, *J. Alloys Compd.* 970 (2024).
- [20] D. Cui, Z. Yang, B. Guo, L. Liu, Z. Wang, J. Li, J. Wang, F. He, Microstructures and mechanical properties of a precipitation hardened refractory multi-principal element alloy, *Intermetallics* 151 (2022).
- [21] Q. Li, X. Li, C. Jin, H. Li, K. Hua, X. Deng, H. Wang, Trace B doping Fe₅₀Mn₃₀Co₁₀Cr₁₀ high entropy alloy: mechanical response and multi-microstructure evolution under TWIP and TRIP effects, *Mater. Sci. Eng., A* 873 (2023).

- [22] G. Li, J. Jiang, H. Ma, R. Zheng, S. Gao, S. Zhao, C. Ma, K. Ameyama, B. Ding, X. Li, Superior strength-ductility synergy in three-dimensional heterogeneous-nanostructured metals, *Acta Mater.* 256 (2023).
- [23] E. Ma, C. Liu, Chemical inhomogeneities in high-entropy alloys help mitigate the strength-ductility trade-off, *Prog. Mater. Sci.* 143 (2024).
- [24] Y. Bai, K. Zhang, T. Chen, Z. Liu, Y. Wang, B. Wei, Alterable tension-compression asymmetry in work hardening of an additively manufactured dual-phase high-entropy alloy, *Int. J. Plast.* 158 (2022).
- [25] Y.L. Zhao, Y.R. Li, G.M. Yeli, J.H. Luan, S.F. Liu, W.T. Lin, D. Chen, X.J. Liu, J. Kai, C.T. Liu, T. Yang, Anomalous precipitate-size-dependent ductility in multicomponent high-entropy alloys with dense nanoscale precipitates, *Acta Mater.* 223 (2022).
- [26] H.G. Li, Y.J. Huang, W.J. Zhao, T. Chen, J.F. Sun, D.Q. Wei, Q. Du, Y.C. Zou, Y. Z. Lu, P. Zhu, X. Lu, A.H.W. Ngan, Overcoming the strength-ductility trade-off in an additively manufactured CoCrFeMnNi high entropy alloy via deep cryogenic treatment, *Addit. Manuf.* 50 (2022).
- [27] W. Wang, Z. Zhang, J. Niu, H. Wu, S. Zhai, Y. Wang, Effect of Al addition on structural evolution and mechanical properties of the Al_xHfNbTiZr high-entropy alloys, *Mater. Today Commun.* 16 (2018) 242–249.
- [28] Y. Zhang, B. Qin, D. Ouyang, L. Liu, C. Feng, Y. Yan, S. Ye, H. Ke, K.C. Chan, W. Wang, Strong yet ductile refractory high entropy alloy fabricated via additive manufacturing, *Addit. Manuf.* 81 (2024).
- [29] Q. Li, H. Zhang, D. Li, Z. Chen, F. Wang, M. Wu, Comparative study of the microstructures and mechanical properties of laser metal deposited and vacuum arc melted refractory NbMoTa medium-entropy alloy, *Int. J. Refract. Met. Hard Mater.* 88 (2020).
- [30] E. Plancher, C.C. Tasan, S. Sandlöbes, D. Raabe, On dislocation involvement in Ti-Nb gum metal plasticity, *Scripta Mater.* 68 (10) (2013) 805–808.
- [31] J. Ren, M. Wu, C. Li, S. Guan, J. Dong, J.-B. Forien, T. Li, K.S. Shanks, D. Yu, Y. Chen, K. An, K.Y. Xie, W. Chen, T. Voisin, W. Chen, Deformation mechanisms in an additively manufactured dual-phase eutectic high-entropy alloy, *Acta Mater.* 257 (2023).
- [32] Z. Liu, R. Li, D. Chen, Y. Sun, B. He, Y. Zou, Enhanced tensile ductility of an additively manufactured near- α titanium alloy by microscale shear banding, *Int. J. Plast.* 157 (2022).
- [33] D. Cui, Y. Zhang, L. Liu, Y. Li, L. Wang, Z. Wang, J. Li, J. Wang, F. He, Oxygen-assisted spinodal structure achieves 1.5 GPa yield strength in a ductile refractory high-entropy alloy, *J. Mater. Sci. Technol.* 157 (2023) 11–20.
- [34] S. Wei, S.J. Kim, J. Kang, Y. Zhang, Y. Zhang, T. Furuhara, E.S. Park, C.C. Tasan, Natural-mixing guided design of refractory high-entropy alloys with as-cast tensile ductility, *Nat. Mater.* 19 (11) (2020) 1175–1181.
- [35] Y. Bu, Y. Wu, Z. Lei, X. Yuan, H. Wu, X. Feng, J. Liu, J. Ding, Y. Lu, H. Wang, Z. Lu, W. Yang, Local chemical fluctuation mediated ductility in body-centered-cubic high-entropy alloys, *Mater. Today* 46 (2021) 28–34.
- [36] Z. An, S. Mao, Y. Liu, L. Wang, H. Zhou, B. Gan, Z. Zhang, X. Han, A novel HfNbTaTiV high-entropy alloy of superior mechanical properties designed on the principle of maximum lattice distortion, *J. Mater. Sci. Technol.* 79 (2021) 109–117.
- [37] S. Wang, M. Wu, D. Shu, B. Sun, Kinking in a refractory TiZrHfNb0.7 medium-entropy alloy, *Mater. Lett.* 264 (2020).
- [38] Y. Liu, Y. Li, Q. Zhu, H. Zhang, X. Qi, D. Zheng, Y. Li, D. Zhang, X. Zeng, Kinking-facilitated nano-crystallization in a shock compressed Mg-1Zn alloy, *J. Magnesium Alloys* 11 (4) (2023) 1162–1169.
- [39] M. Yamasaki, K. Hagihara, S.-I. Inoue, J.P. Hadorn, Y. Kawamura, Crystallographic classification of kink bands in an extruded Mg-Zn-Y alloy using intragranular misorientation axis analysis, *Acta Mater.* 61 (6) (2013) 2065–2076.
- [40] D. Cui, X. Bai, X. Liu, Y. Qiu, Z. Wang, J. Li, J. Wang, F. He, Kinking induced plasticity in a novel refractory high-entropy alloy, *Vacuum* 227 (2024).
- [41] G. Dirras, H. Couque, L. Lilienstern, A. Heczel, D. Tingaud, J.P. Couzinié, L. Perrière, J. Gubicza, I. Guillot, Mechanical behavior and microstructure of Ti₂₀Hf₂₀Zr₂₀Ta₂₀Nb₂₀ high-entropy alloy loaded under quasi-static and dynamic compression conditions, *Mater. Char.* 111 (2016) 106–113.
- [42] R.R. Eleti, N. Stepanov, N. Yurchenko, S. Zherebtsov, F. Maresca, Cross-kink unpinning controls the medium- to high-temperature strength of body-centered cubic NbTiZr medium-entropy alloy, *Scripta Mater.* 209 (2022).
- [43] S. Yao, X. Pei, J. Yu, Q. Wu, Assessment of the time-dependent behavior of dislocation multiplication under shock loading, *Int. J. Plast.* 158 (2022).
- [44] L.L. Hsiung, On the mechanism of anomalous slip in bcc metals, *Mater. Sci. Eng., A* 528 (1) (2010) 329–337.
- [45] C. Marichal, H. Van Swygenhoven, S. Van Petegem, C. Borca, {110} Slip with {112} slip traces in bcc Tungsten, *Sci. Rep.* 3 (1) (2013).
- [46] X. Yan, P.K. Liaw, Y. Zhang, Ultrastrong and ductile BCC high-entropy alloys with low-density via dislocation regulation and nanoprecipitates, *J. Mater. Sci. Technol.* 110 (2022) 109–116.
- [47] S. Sadeghpour, S.M. Abbasi, M. Morakabati, L.P. Karjalainen, Effect of dislocation channeling and kink band formation on enhanced tensile properties of a new beta Ti alloy, *J. Alloys Compd.* 808 (2019).
- [48] X. Yan, Y. Zhang, A body-centered cubic Zr₅₀Ti₃₅Nb₁₅ medium-entropy alloy with unique properties, *Scripta Mater.* 178 (2020) 329–333.